Scripta Materialia 114 (2016) 146–150

Contents lists available at ScienceDirect

Scripta Materialia

journal homepage: www.elsevier.com/locate/scriptamat

Regular Article

High-energy synchrotron study of in-pile-irradiated U–Mo fuels

Yinbin Miao [a,*], Kun Mo [a], Bei Ye [a], Laura Jamison [a], Zhi-Gang Mei [a], Jian Gan [b], Brandon Miller [b], James Madden [b], Jun-Sang Park [a], Jonathan Almer [a], Sumit Bhattacharya [c], Yeon Soo Kim [a], Gerard L. Hofman [a], Abdellatif M. Yacout [a]

[a] Argonne National Laboratory, Lemont, IL 60439, United States
[b] Idaho National Laboratory, Idaho Falls, ID 83415, United States
[c] Northwestern University, Evanston, IL 60208, United States

ARTICLE INFO

Article history:
Received 30 October 2015
Received in revised form 4 December 2015
Accepted 13 December 2015
Available online xxxx

Keywords:
X-ray diffraction
Synchrotron radiation
Superlattice
Recrystallization
Metallic nuclear fuel

ABSTRACT

Here synchrotron scattering analysis results on U–7wt.%Mo fuel specimens irradiated in the Advanced Test Reactor to three burnup levels (3.0, 5.2, and 6.3 × 10^{21} fission/cm^3) are reported. Mature fission gas bubble superlattice was observed to form at intermediate burnup. The superlattice constant was determined to be 11.7 and 12.0 nm by wide-angle and small-angle scattering respectively. Grain sub-division takes place throughout the irradiation and causes the collapse of the superlattice at high burnup. The bubble superlattice expands the U–Mo lattice and acts as strong sink for radiation-induced defects. The evolution of dislocation loops was, therefore, suppressed until the bubble superlattice collapsed.

The decades-long campaign of the Reduced Enrichment for Research and Test Reactors (RERTR), later to be known as the Global Threat Reduction Initiative (GTRI), and the successive Material Management and Minimization (M^3) programs aims to replace high-enriched-uranium (HEU) fuels with low-enriched-uranium (LEU) fuels in research reactors in order to minimize the risk of nuclear proliferation [1]. The realization of this task relies on the successful development of nuclear fuel materials with high uranium density [2]. Among high-uranium materials, the U–Mo alloy system has become a strong candidate fuel for the conversion of high power research reactors due to impressive in-pile performance [3–6]. The trials of developing U–Mo fuels involve both monolithic and dispersed forms of fuel plates [7,8]. For those dispersion U–Mo fuel plates, U–Mo particles are dispersed in an Al matrix to form fuel "meat", which is further clad in Al alloy.

Fission gas behavior, gas swelling in particular, affects multiple key properties of the fuel, and, hence, remains the key component for nuclear fuel material characterization. As such, it is important to investigate the evolution of the fuel microstructure (including bubble morphology) during burnup in order to better understand the fundamental mechanisms involved in the degradation of fuel performance [9]. According to previous transmission electron microscopy (TEM) observations of the U–7wt.%Mo dispersion fuels irradiated in the Advanced Test Reactor (ATR) [10], nanoscale fission gas bubbles form a face-centered cubic (FCC) superlattice at intermediate burnup (see Fig. 1(a)), which collapses into microscale fission bubbles due to grain sub-division at high burnup. The grain sub-division reduces the grain size from the micron scale to 100–500 nm [11,12,13,10]. While TEM observation provides direct microscopic images of the irradiated fuel structures, this technique is limited to only a few grains. To quantify microstructural information, in addition to the bubble superlattice morphology, bulk measurement is critical for precise interpretation of the U–7wt.%Mo's fuel performance. In recent examinations of out-of-pile U–Mo fuels, synchrotron scattering techniques have proven to be powerful tools in accomplishing this task [14–16]. In this regard, a coordinated experiment combining synchrotron wide-angle and small-angle X-ray scattering (WAXS/SAXS) was carried out to comprehensively study the microstructural features of U–7wt.%Mo dispersion fuel at different burnup levels.

The U–7wt.%Mo specimens examined in this study were irradiated in the ATR up to 6.3 × 10^{21} fission/cm^3 [10], as a part of the RERTR-7 irradiation campaign. Detailed sample information can be found in Table 1. Sample O is the control sample, which was not irradiated. Each sample was fabricated by focused ion beam (FIB) milling into an approximately 30 μm × 30 μm × 30 μm cube by an FEI QUANTA 3D FIB system, and then mounted onto a W omniprobe using Pt welding. The sample selection regions were carefully limited within the U–7wt.%Mo fuel particles, to avoid any interference from the matrix or interaction layer. The omniprobes were loaded in a double containment sample holder fabricated from Kapton tubes for the synchrotron investigation. The synchrotron investigation was performed at Sector 1-ID,

* Corresponding author at: 9700 S Cass Ave, Argonne, IL 60439, United States.
E-mail address: ymiao@anl.gov (Y. Miao).

http://dx.doi.org/10.1016/j.scriptamat.2015.12.019
1359-6462/

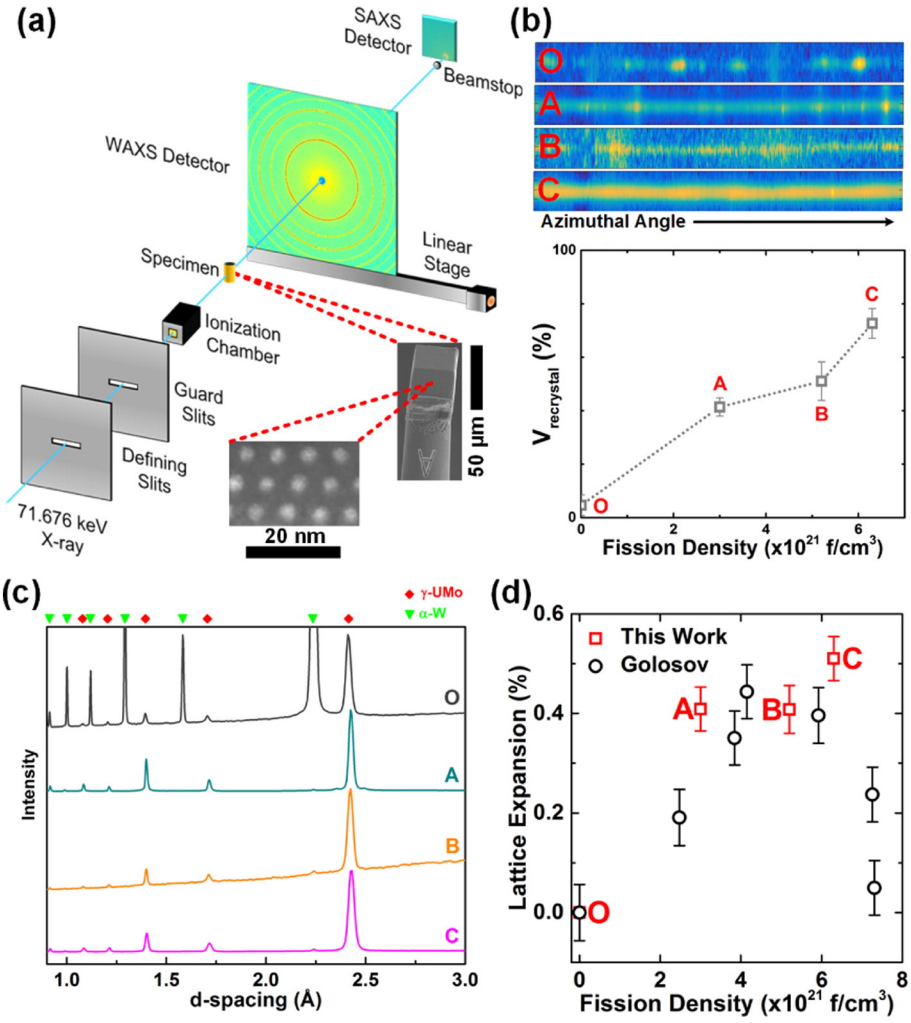

Fig. 1. General WAXS results: (a) basic setup of the synchrotron experiment with a scanning electron microscope (SEM) image of a sample cube mounted on a W omniprobe, and a TEM image of the fission gas bubble superlattice in Sample A [10]; (b) the azimuth distribution of the {110} peak of γ-U–Mo phase, along with the volume fraction evolution of recrystallized grains; (c) azimuthally integrated WAXS lineouts; (d) expansion of the lattice parameter of γ-U–Mo under irradiation, compared with Golosov et al.'s results [30].

Advanced Photon Source (APS), Argonne National Laboratory (ANL). As shown in Fig. 1(a), a 10 μm × 10 μm monochromatic (71.676 keV) X-ray beam was utilized to illuminate the U–7wt.%Mo samples for the X-ray scattering experiment. The WAXS patterns were collected by a GE Revolution 41RT panel detector with a 41 cm × 41 cm detection area and 200 μm × 200 μm pixel size. Separately taken were the SAXS data by a 31 mm × 25 mm Pixirad detector with 60 μm hexagonal pixels. Among the four samples, Sample B had a relatively low volume, resulting in a weaker X-ray scattering signal and larger statistical errors.

The changes in lattice spacing were measured by averaging the d-spacing evolution of the reflection peaks. The volume fraction of recrystallization-induced sub-division of grains was determined by counting the integrated intensities of the diffraction peaks from either the large-sized original grains or the small-sized recrystallized grains. Both original and modified Williamson–Hall (W–H) analyses were conducted to attain the internal strain/dislocation density information from the broadening of diffraction peaks[17]. In the original W–H method, the breadth of diffraction peaks was interpreted to be from the combined effect of internal strain and grain size:

$$\beta\cos\theta = C\varepsilon\sin\theta + K\lambda/D, \tag{1}$$

where β is the breadth of a specific reflection peak, θ is the diffraction angle, ε is the internal strain, λ is the wavelength of the photon, D is the grain size, and C and K are adjustable constants. On the other hand, when the internal strain is assumed to be dominated by dislocations, the modified W–H method can be applied to determine the dislocation density within the diffraction volume:

$$\Delta K = 0.9/D + \left(\pi A^2 b^2/2\right)^{\frac{1}{2}}\rho^{\frac{1}{2}}\left(K\bar{C}^{\frac{1}{2}}\right), \tag{2}$$

where A is an adjustable parameter ranging from 1 to 2, b is the length of Burgers vector, ρ is the dislocation density, $\bar{C}$ is the contrast factor, $K = 2\sin\theta/\lambda$, $\Delta K = 2\cos\theta\Delta\theta/\lambda$. $\bar{C}$ is determined by the crystal structure and stiffness tensor of the material [18]. The stiffness tensor of U–7wt.%Mo was predicted by first principle calculation (c_{11} = 174.51 GPa, c_{12} = 107.71 GPa and c_{44} = 49.52 GPa) using Vienna Ab-initio Simulation Package (VASP). More details of the W–H analysis and other related synchrotron scattering techniques can be found in Refs. [19–23]. In

Table 1
List of samples investigated in this study.

Sample index	O	A	B	C
Fuel plate ID	n/a	R3R050 (low)	R3R050 (high)	R2R040
Burnup (×10^{21} f/cm^3)	0.0	3.0	5.2	6.3

addition, the Guinier approximation [24] was first employed for the analysis of the SAXS data:

$$I(Q) = I_0 \exp\left(-R_g^2 Q^2/3\right) \tag{3}$$

where $Q = 4\pi \sin\theta/\lambda$ is the length of the scattering vector, I_0 is the reference intensity, $I(Q)$ is the intensity at Q, and R_g is radius of gyration. More detailed SAXS data analysis was performed by IRENA package [25], assuming the fission gas bubbles are unified sphere shapes [26]. That is, these bubbles have the following form factor (F):

$$F^2(Q) = \exp\left(-R_g^2 Q^2/3\right) + \frac{1.62}{R_g^4}\left[\frac{erf^3\left(QR_g/\sqrt{6}\right)}{Q}\right]^4. \tag{4}$$

The fitting of SAXS data was based on the maximum entropy algorithm [27,28] so that the size distribution of the bubbles could be assessed.

In WAXS data, only two phases, γ-U–Mo (the original phases in the unirradiated material) and α-W, were identified in all four samples, as indicated in Fig. 1(c). Tungsten signals came from the omniprobes holding the samples. This indicates the high stability of γ phase in U–7wt.%Mo where no additional α phase was produced under ATR irradiation conditions. Meanwhile, the 2-D X-ray detector precisely captured the recrystallization-induced grain sub-division phenomenon [29]. In the control sample (O), the majority of the diffraction (over 95%) is contributed by large-sized grains. As burnup rises, the contribution of small-sized recrystallized grains increases with burnup to over 70% in Sample C, as illustrated by Fig. 1(b). In addition, as illustrated by Fig. 1(d), the lattice constant of γ-U–Mo rises steeply at low burnup (from O to A), and then increases slightly (from A through B to C). The results are comparable to Golosov et al.'s U–9wt.%Mo report [30].

Satellite peaks were observed near all the diffraction peaks of U–Mo in Sample A. These satellite peaks not only indicate the existence of the fission gas bubble superlattice, but also demonstrate that the orientations of a U–Mo grain and the associated superlattice are related. Another important discovery is that these satellite peaks are only present around the diffraction peaks of large-sized grains, and are absent near the peaks of recrystallized grains (see Fig. 2(b)), indicating that the bubble superlattice was eliminated in the recrystallized grains. In fact, with the evolution of grain sub-division, the satellite peaks could only be found near the diffraction peaks of those limited number of remaining large-sized grains in Sample B, see Fig. 2(c). As burnup arrives at 6.3×10^{21} fission/cm^3 in Sample C, satellite peaks were not found due to the absence of large-sized grains. Since many grains are interrogated simultaneously by the X-ray, the 2D WAXS detector collects diffraction information from a larger number of grains rather than a handful of grains interrogated by TEM. Therefore, the investigation of the superlattice using WAXS data differs from the one based on electron diffraction. The azimuth integration of the Debye–Scherrer rings is used, rather than separate diffraction spots. However, the diffraction vectors of the bubble superlattice are not necessarily perpendicular to the azimuth direction. As a result, the satellite peaks on azimuth integrated profiles actually correspond to the projected positions of the satellite spots. Hence, in order to correctly interpret the satellite peaks observed in WAXS investigations and precisely measure the superlattice constant, this projection effect must be taken into consideration, as shown in Fig. 2(a), (g) and (h). Based on the WAXS data, the superlattice constant (a_{SL}) was determined to be 11.7 ± 0.2 nm (see Fig. 2). This value is comparable with the previous TEM observations (12.0 nm) [10]. In addition, satellite peak information also confirms the TEM observations that the

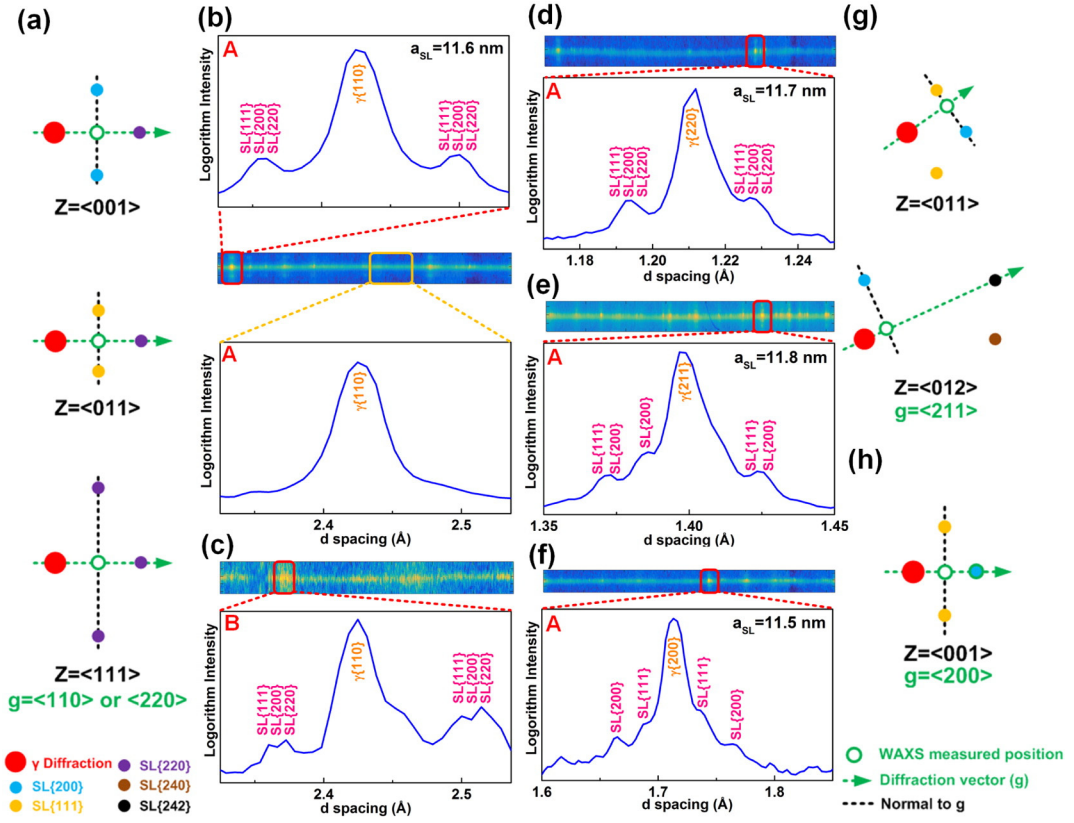

Fig. 2. The satellite peaks around the diffraction peaks in WAXS results: (a)/(g)/(h) positions of the satellite peaks near {110} ({220}), {211} and {200} reflections, respectively; (b) the presence of satellite peaks around the {110} reflection contributed by original large grains (upper) and the absence of satellite peaks around the {110} reflection contributed by recrystallized small grains (lower) in Sample A; (c) the satellite peaks near {110} reflections from remaining bubble superlattice in Sample B; (d)/(e)/(f) the satellite peaks contributed by original large grains around the {220}, {211} and {200} reflections, respectively, in Sample A. (SL stands for superlattice.)

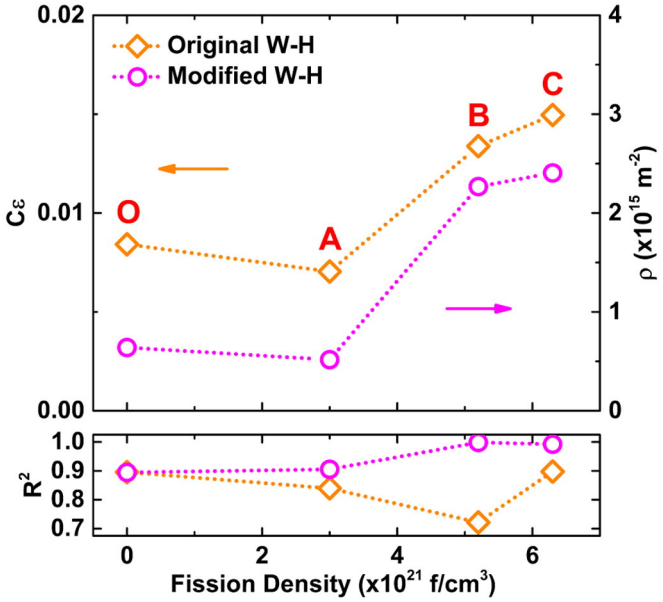

Fig. 3. The Williamson–Hall (W–H) analyses: the internal strain ($C\varepsilon$) and dislocation density (ρ) evolution deduced by the original and modified W–H analyses respectively. The lower R^2 values of the original W–H fittings imply that the modified W–H analysis is a better interpretation for diffraction peak broadening in in-pile-irradiated U–Mo specimens.

superlattice structure is FCC, according to the extinction criteria, and that the orientation relationship between the matrix and the superlattice is cubic-on-cubic (CoC), referring to the projected positions.

Both original and modified W–H analyses were performed on the U–7wt.%Mo samples. As the grain size in those samples exceeds the detector limit, which is approximately 100 nm in the current experimental condition, only the internal strains or dislocation densities were quantified in the present study. Fig. 3 illustrates the evolution of the internal strain and dislocation density with increasing burnup along with the measure of goodness-of-fit, R^2. Both quantities slightly decrease at intermediate burnup (A), probably due to local fluctuation, and then continue to increase with burnup. The good linearity of the modified W–H fitting demonstrates that the isotropically distributed dislocations account for the majority of the contributions to peak broadening due to internal strain, especially for Samples B and C.

Satellite peaks near the transmitted beam were also captured by the SAXS detector. Two sets of superlattice reflections of low indices, {111} and {200}, were found in Sample A, indicating a superlattice constant of 12.0 ± 0.2 nm, as shown in Fig. 4(a). This measurement is more accurate than the WAXS-based values in this study because the satellite peaks around the transmitted beam are free from the interference caused by broadened γ diffraction peaks. The extinction of the {110} peak further confirms the FCC superlattice structure. Satellite peaks were not observed on the SAXS detector in Samples O, B, and C. In addition, the azimuthally integrated curve of SAXS data contains information about the size of randomly distributed bubbles. In fact, the SAXS data from both Samples O and A have no distinguishable Guinier regions. In Sample O, there are no fission gas bubbles. In Sample A, the well-aligned bubble superlattice contributes to diffraction at small angle rather than a Guinier region. However, in Sample C, the Guinier fitting gives a radius of gyration around 11.3 nm, corresponding to a diameter around 29.2 nm, which is much larger than the bubbles in the superlattice (4 nm). Further maximum entropy fitting shows that the bubble size ranges from approximately 20 nm up to 100 nm with a maximum approximately at 35 nm, as illustrated in Fig. 4(b). It is worth mentioning that a peak was observed in a small-angle neutron scattering (SANS) investigation of in-pile irradiated U–9wt.%Mo samples, and was interpreted as the formation of Guinier-Preston zones [31]. That peak might also be related to the bubble superlattice, although the Q position of that peak (0.08 $Å^{-1}$) is off the observations in this study (0.091 $Å^{-1}$ for {111} and 0.105 $Å^{-1}$ for {200}).

Coordinated WAXS and SAXS investigations clearly indicate that a mature CoC FCC bubble superlattice is formed at intermediate burnup in U–7wt.%Mo samples irradiated in the ATR. The superlattice formation might be explained by interbubble elastic interactions, planar diffusion of host interstitials, or interactions between bubble-punched dislocations [32]. With increasing burnup, the consequential recrystallization and grain sub-division result in the collapse of the bubble superlattice. After the superlattice collapse, in addition to the large bubbles (over 100 nm in diameter) that were observed by TEM [10], intermediate-sized bubbles (around 35 nm) also exist in the recrystallized grains according to the SAXS data. There exists a high initial dislocation density in the control sample, mainly induced by the mechanical work during fuel plate manufacturing process. At intermediate burnup, the formation of a bubble superlattice expands the U–Mo lattice, creating strong defect sinks that suppress the nucleation and growth of dislocation loops. At high burnup, the collapse of the bubble superlattice releases the internal stress and initiates the precipitation of solid fission products on the surfaces of large bubbles [10], relieving the lattice expansion. Compared to the neutron scattering data [30], the fact that the lattice constant does not drop in Sample C might originate from the relatively insufficient burnup (6.3×10^{21} fission/cm^3 compared to 7.3×10^{21} fission/cm^3), and local fluctuation of the Mo content [33] due to the relatively limited illuminated volumes in synchrotron scattering (micron level compared to millimeter level). Meanwhile, in the

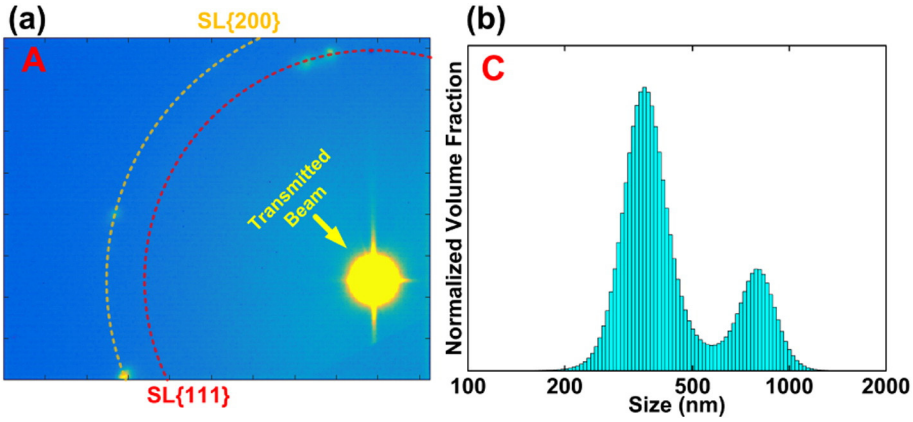

Fig. 4. SAXS results: (a) SAXS data showing the satellite peaks near the transmitted beam of Sample A; (b) bubble size distribution determined by SAXS fitting using unified sphere model. (SL stands for superlattice.)

absence of the bubble superlattice as a sink for defects, dislocation loops were generated and accumulated significantly, and were found to be the dominant origin of diffraction peak broadening at elevated burnups.

In summary, U–7wt.%Mo fuel samples were irradiated to various burnup levels, and investigated by synchrotron scattering. A mature fission gas bubble superlattice was confirmed to be present at intermediate burnup, and then the superlattice constant was measured to be 11.7 and 12.0 nm by WAXS and SAXS, respectively. The bubble superlattice was found to act as a strong sink for radiation-induced defects, suppressing the evolution of dislocation loops. Radiation-induced recrystallization and consequent grain sub-division, continuously take place after burnup exceeds the threshold, eventually causing the bubble superlattice to collapse. Once the bubble superlattice structure was eliminated, the nucleation and growth of dislocation loops increased five fold. In this study, synchrotron X-ray scattering was used for the first time to study in-pile irradiated U–Mo fuel as a function of burnup. Various microstructural modifications were quantitatively characterized to provide a systematic microstructure evolution mechanism in in-pile-irradiated U–7wt.%Mo. This knowledge will help establish precise methods for the fuel performance prediction of the U–Mo system and consequently advance the M^3 program.

This research was sponsored by the U.S. Department of Energy, National Nuclear Safety Administration (NNSA), Office of Material Management and Minimization (NA-23) Reactor Conversion Program. This research used the resources of the Advanced Photon Source, a U.S. Department of Energy (DOE) Office of Science User Facility operated for the DOE Office of Science by Argonne National Laboratory. Both programs are supported under Contract No. DE-AC-02-06CH11357 between UChicago Argonne, LLC and the U.S. Department of Energy.

Appendix A. Supplementary data

Supplementary data to this article can be found online at http://dx.doi.org/10.1016/j.scriptamat.2015.12.019.

References

[1] A. Travelli, International RERTR Meeting, 2003.
[2] J.L. Snelgrove, G. Hofman, M. Meyer, C. Trybus, T. Wiencek, Nucl. Eng. Des. 178 (1997) 119–126.
[3] K.H. Kim, D.B. Lee, C.K. Kim, G.E. Hofman, K.W. Paik, J. Nucl. Mater. 245 (1997) 179–184.
[4] G.L. Hofman, M.K. Meyer, A. Ray, Proceedings of the 1998 International Reduced Enrichment for Test Reactor Conference, 1998.
[5] M. Meyer, G. Hofman, S. Hayes, C. Clark, T. Wiencek, J. Snelgrove, R. Strain, K.-H. Kim, J. Nucl. Mater. 304 (2002) 221–236.
[6] Y. Miao, B. Beeler, C. Deo, M.I. Baskes, M.A. Okuniewski, J.F. Stubbins, J. Nucl. Mater. 456 (2015) 1–6.
[7] M. Meyer, J. Gan, J. Jue, D. Keiser, E. Perez, A. Robinson, D. Wachs, N. Woolstenhulme, G. Hofman, Y. Kim, Nucl. Eng. Technol. 46 (2014) 169–182.
[8] Y.S. Kim, G. Hofman, A. Robinson, D. Wachs, Nucl. Technol. 184 (2013) 42–53.
[9] B. Ye, S. Bhattacharya, K. Mo, D. Yun, W. Mohamed, M. Pellin, J. Fortner, Y. Kim, G. Hofman, A. Yacout, et al., J. Nucl. Mater. 464 (2015) 236–244.
[10] B. Miller, J. Gan, D. Keiser, A. Robinson, J. Jue, J. Madden, P. Medvedev, J. Nucl. Mater. 458 (2015) 115–121.
[11] S. Van den Berghe, W. Van Renterghem, A. Leenaers, J. Nucl. Mater. 375 (2008) 340–346.
[12] J. Gan, D. Keiser, D.M. Wachs, A.B. Robinson, B.D. Miller, T.R. Allen, J. Nucl. Mater. 396 (2010) 234–239.
[13] J. Gan, D. Keiser, B.D. Miller, A.B. Robinson, J.-F. Jue, P. Medvedev, D.M. Wachs, J. Nucl. Mater. 424 (2012) 43–50.
[14] D. Brown, M. Okuniewski, J. Almer, L. Balogh, B. Clausen, J. Okasinski, B. Rabin, J. Nucl. Mater. 441 (2013) 252–261.
[15] D. Brown, D. Alexander, K. Clarke, B. Clausen, M. Okuniewski, T. Sisneros, Scr. Mater. 69 (2013) 666–669.
[16] H. Palancher, N. Wieschalla, P. Martin, R. Tucoulou, C. Sabathier, W. Petry, J.-F. Berar, C. Valot, S. Dubois, J. Nucl. Mater. 385 (2009) 449–455.
[17] T. Ungár, Materials Science Forum, vol. 278, Trans Tech Publications, Parma, Italy 1997, pp. 151–157.
[18] T. Ungár, I. Dragomir, Á. Révész, A. Borbély, J. Appl. Crystallogr. 32 (1999) 992–1002.
[19] Y. Miao, K. Mo, Z. Zhou, X. Liu, K.-C. Lan, G. Zhang, M.K. Miller, K.A. Powers, J. Almer, J.F. Stubbins, Mater. Sci. Eng. A 625 (2015) 146–152.
[20] Y. Miao, K. Mo, Z. Zhou, X. Liu, K.-C. Lan, G. Zhang, M.K. Miller, K.A. Powers, Z.-G. Mei, J.-S. Park, et al., Mater. Sci. Eng. A (2015).
[21] Y. Miao, K. Mo, B. Cui, W.-Y. Chen, M.K. Miller, K.A. Powers, V. McCreary, D. Gross, J. Almer, I.M. Robertson, et al., Mater. Charact. 101 (2015) 136–143.
[22] K. Mo, Z. Zhou, Y. Miao, D. Yun, H.-M. Tung, G. Zhang, W. Chen, J. Almer, J.F. Stubbins, J. Nucl. Mater. 455 (2014) 376–381.
[23] P. Mosbrucker, D. Brown, O. Anderoglu, L. Balogh, S. Maloy, T. Sisneros, J. Almer, E. Tulk, W. Morgenroth, A. Dippel, J. Nucl. Mater. 443 (2013) 522–530.
[24] A. Guinier, G. Fournet, J. Wiley & Sons, New York (1955).
[25] J. Ilavsky, P.R. Jemian, J. Appl. Crystallogr. 42 (2009) 347–353.
[26] G. Beaucage, J. Appl. Crystallogr. 28 (1995) 717–728.
[27] P. Jemian, G. Long, F. Lofaj, S. Wiederhorn, MRS Proceedings, volume 590, Cambridge Univ Press, 1999, p. 131.
[28] J. Potton, G. Daniell, B. Rainford, J. Appl. Crystallogr. 21 (1988) 663–668.
[29] Y.S. Kim, G. Hofman, J. Cheon, J. Nucl. Mater. 436 (2013) 14–22.
[30] O. Golosov, M. Lyutikova, V. Semerikov, A.Y. Teplykh, RRFM 2008 Transactions, 2008 (02–3).
[31] O. Golosov, V. Semerikov, S. Bogdanov, M. Lyutikova, Technical Report, Argonne National Laboratory, Nuclear Engineering Division, RERTR Department, Argonne, IL (United States); Czech Technical University, Prague (Czech Republic), 2008.
[32] P. Johnson, K. Stevens, R. Thomson, Nucl. Inst. Methods Phys. Res. B 62 (1991) 218–227.
[33] A. Landa, P. Söderlind, P. Turchi, J. Nucl. Mater. 414 (2011) 132–137.